 CMES, vol.95, no.4, pp.317-349, 2013

A Self-regularization Technique in Boundary Element Method for 3-D Stress Analysis

M. G. He[1] **and C.L. Tan**[1]

Abstract: The self-regularization technique in the Boundary Element Method (BEM) originally proposed by Cruse and Richardson (1996, 1999) in their work for two-dimensional (2-D) stress analysis is extended to three-dimensional (3-D) elastostatics in this paper. The regularization scheme addresses the issue of accurate numerical evaluation of the integrals due to the singularity of the kernel functions of the integral equations. It is first implemented for the determination of displacements and stresses at interior points of the solution domain, and very accurate results are obtained even when these points are very close to the surface of the domain. A self-regularized traction-BIE is then implemented with two different approaches to deal with the requirement of continuity of the displacement-gradients across element boundaries. The examples presented suggest that when corners are present, this smoothness requirement for the traction-BIE must be met if convergence of the solution is to be assured. Finally, a self-regularized displacement-BIE is developed which can treat thin-body problems by eliminating the near-singularity issues encountered in conventional BEM. This is demonstrated by numerical examples.

Keywords: Boundary Element Method, self-regularization, near-singularity, thin-body problems

1 Introduction

The Boundary Element Method (BEM) is based on boundary integral equations (BIE), which are derived using the fundamental solutions (or Green's functions) to the governing differential equations and the reciprocal work theorem. These fundamental solutions, which form the kernel functions of the BIE, are singular with respect to the distance between the source point and the field point on the

[1] Corresponding author. Email: choonlai.tan@carleton.ca
Department of Mechanical & Aerospace Engineering, Carleton University, Ottawa, Canada K1S 5B6.

surface of the solution domain. The variations of the numerical values of the kernels can be very rapid over the surface close to the source point. This near-singularity problem mainly occurs in two situations in BEM analysis, namely: a) determination of interior point solutions when these points are close to the surface of the domain, and b) thin-body problems where two parts of the surface are close to each other.

A direct way of reducing singularity occurring in interior point solutions is to refine the surface mesh near the interior point, or to significantly increase the number of Gauss points, as can be seen in Li (2003). This approach, however, greatly increases the number of elements used and hence the computational effort, especially when numerous interior points are involved. It will be cumbersome indeed in 3-D analysis. Other methods of removing the singularity include "regularization", see, e.g. Granados and Gallego (2001); Ma and Kamiya (2001); Niu, Wendland, Wang and Zhou (2005); Zhou, Niu, Cheng and Guan (2008); Xie, Zhang, Qin and Li (2011). These approaches have been shown to provide very accurate results in two dimensions, but they are either analytically complex and/or the numerical algorithm, difficult to apply to general 3-D problems. A scheme was proposed by Cruse and Richardson (1996) and Richardson and Cruse (1999) in their 2-D analysis, in which simple solutions are subtracted and added back into the Somigliana's identities for interior point displacements and stresses, respectively. This method is relatively simple both analytically and in the numerical implementation, as compared to the other schemes. It has been employed, e.g. Li (2003); Shah, Tan and Wang (2006), for the determination of T-stress in fracture mechanics where interior point solutions are calculated on an integration path which can be very close to the crack surface. In the next Section, this technique is extended to BEM for 3-D elastostatics.

The methods proposed in the literature to solve thin-body problems are mostly to analytically integrate the singular kernels, see e.g., Ye and Liu (1985), Liu (1987), Krishnasamy, Rizzo and Liu (1994). In Liu (1998), a non-degeneracy approach is proposed by adding and subtracting a term to the conventional displacement-BIE which was then transformed into line-integrals using Stoke's theorem and evaluated analytically. Cruse and Aithal (1993) also proposed a scheme using regularization of integral operators and a theta integration algorithm. All these approaches are, again, mathematically quite involved and are less than simple to implement especially in three dimensions.

Cruse and Richardson (1996) and Richardson and Cruse (1999) also obtained the self-regularized traction-BIE by taking the interior point to the boundary in Somigliana's stress identity. They suggested that this scheme is well-suited for thin-body problems. It will be therefore tested in this study in 3-D. An issue with this scheme is the requirement of continuity in the displacement gradients or stresses across

element boundaries, i.e. $C^{1,\alpha}$ Holder continuity; this is discussed in Martin and Rizzo (1996); Martin, Rizzo and Cruse (1998). In conventional BIE, the most commonly used quadratic elements are only $C^{0,\alpha}$ continuous. It should be noted that self-regularization of the BIE has been proposed before, see, e.g. Rudolphi (1991); Sladek, Sladek and Tanaka (1993); Matsumoto and Tanaka (1993); Frangi and Guigianni (2001); Dong and Atluri (2012) The algorithm proposed in Cruse and Richardson (1996) is significantly easier to implement, and it uses only $C^{0,\alpha}$ conforming boundary elements throughout, However, its theoretical validity has been questioned, as mentioned above, since the smoothness requirement of at least $C^{1,\alpha}$ at the source points for the hypersingular integrals is not met. Several researchers have dealt with this issue, although, mostly in the 2-D case (see, e.g. Jorge, Cruse, Fisher and Ribeiro (2003); Wang and Li (2009); Jin, Zhang, Wang and Li (2011)) in their attempts to enforce the continuity of displacement-gradients across element boundaries. Notwithstanding the efficiency and the accuracy of the solutions that could be obtained, these approaches are evidently not very easy and/or practical to apply in 3-D. A 'relaxed continuity' was proposed in Richardson and Cruse (1999) to use along with the self-regularized traction-BIE. It takes the average of the displacement derivatives at a node according to the element it belongs to. This approach has only been implemented for simple 2-D elasticity problems. A recommendation from this work is to employ higher-order conforming elements beyond the quadratic ones instead, for better convergence. Another approach that has been employed in Gallego and Dominguez (2000) involves the use of non-conforming elements for 2-D elastodynamics. The collocations are done inside the elements, where the $C^{1,\alpha}$ continuity requirement is satisfied, rather than at the boundary nodes. This strategy is also used in 3-D fracture problems where traction-BIE is only applied to elements on the crack surfaces while for all the other elements in the solution domain, the displacement-BIE is applied [Dominguez and Ariza (2000)]. In Section 3, the self-regularized traction-BIE is adopted, along with the relaxed continuity approach and this collocation strategy.

As will be shown in Section 6, the veracity of the algorithm for the traction-BIE with $C^{0,\alpha}$ quadratic, conforming elements is questionable even with the two above-mentioned schemes. This is because the accuracy of the solutions could not be always assured. A self-regularized displacement-BIE is proposed here instead, employing similar notions as for the self-regularized traction-BIE. This will be treated in Section 4 and will be demonstrated in Section 6 to be well-suited for analyzing 3-D thin-body problems. Throughout this study, the standard 8-noded quadrilateral or 6-noded triangular isoparametric elements are used in the numerical BEM formulation. For the evaluation of the integrals over these elements to form the system equations, the standard 4 x 4 Gauss quadrature and the 13-point Hammer-Stroud

quadrature schemes are used, as in the conventional displacement-BEM algorithm.

2 Self-regularization of Somigliana's identities for interior point solutions

The Somigliana's identities for displacements, u_i, and stresses, σ_{ij},at an interior point p of an elastic solid with surface S may be expressed as:

$$u_j(p) = -\int_S T_{ij}(p,Q)u_j(Q)dS(Q) + \int_S U_{ij}(p,Q)t_j(Q)dS(Q) \tag{1}$$

and

$$\sigma_{ij}(p) = -\int_S S_{kij}(p,Q)u_k(Q)dS(Q) + \int_S D_{kij}(p,Q)t_k(Q)dS(Q) \tag{2}$$

where $u_j(Q)$ and $t_j(Q)$ are displacements and tractions at a field point Q on the surface obtained from boundary solutions, and T_{ij}, U_{ij}, S_{kij} and D_{kij} are singular kernels of orders of r^{-2}, r^{-1}, r^{-3} and r^{-2}, respectively, where r is the distance between interior point p and field point Q. The expression of these kernels are well established in the literature, e.g., Cruse (1969). Using the self-regularization proposed in Cruse and Richardson (1996) and Richardson and Cruse (1999), a term corresponding to rigid body motion at a surface point P closest to p is subtracted from Equation (1) while a simple solution corresponding to a constant stress state is subtracted from Equation (2) as follows:

$$u_j(p) - u_j(P) = -\int_S T_{ij}(p,Q)(u_j(Q) - u_j(P)dS(Q) + \int_S U_{ij}(p,Q)t_j(Q)dS(Q) \tag{3}$$

and

$$\begin{aligned}\sigma_{ij}(p) - \sigma_{ij}(P) = &-\int_S S_{kij}(p,Q)[u_k(Q) - u_k^L(Q)]dS(Q) \\ &+ \int_S D_{kij}(p,Q)[t_k(Q) - t_k^L(Q)]dS(Q)\end{aligned} \tag{4}$$

In Equation (4), the constant stress state terms are expressed as:

$$u_k^L(Q) = u_k(P) + u_{k,m}(P)[x_m(Q) - x_m(P)] \tag{5}$$

$$t_k^L(Q) = \sigma_{km}(P)n_m(Q) \tag{6}$$

where $u_{k,m}(P)$ represents the displacement gradients at P, x_m is the global Cartesian coordinate components, and $n_m(Q)$ is the unit outward normal at Q. The regularization point P is chosen as the closest surface point to p.

Equations (3) and (4) have been implemented successfully on simple 2-D problems in Richardson and Cruse (1999). In three dimensions, the singularities of all the

kernels are one order higher than the corresponding ones in 2-D. The kernel U_{ij} in Equation (3) is not regularized since it is only of order of *ln(1/r)* in 2-D and of order r^{-1} in 3-D. Although the associated integral is only weakly singular, it is discovered in this study that this kernel has to be regularized as well in 3-D to obtain accurate results if no adaptive schemes are used in the numerical algorithm. This is due to the increase rate of change of the numerical values of the integrand as r becomes small. Using the same procedure of subtracting and adding back constant stress terms, the following expression is obtained:

$$\begin{aligned} u_j(p) - u_j^L(p) = &- \int_S T_{ij}(p,Q)[u_j(Q) - u_j^L(Q)]dS(Q) \\ &+ \int_S U_{ij}(p,Q)[t_j(Q) - t_j^L(Q)]dS(Q) \end{aligned} \tag{7}$$

where $u_j^L(Q)$ and $t_j^L(Q)$ are given before and $u_j^L(p)$ is defined similarly as:

$$u_j^L(p) = u_j(P) + u_{j,m}(P)[x_m(p) - x_m(P)] \tag{8}$$

where $u_{j,m}(P)$ is again the displacement gradient at P. The relation between tractions and displacement gradients is:

$$t_i = \sigma_{ij} n_j = [\frac{2\mu\upsilon}{1-2\upsilon} u_{k,k}\delta_{ij} + \mu(u_{i,j} + u_{j,i})]n_j \tag{9}$$

The tractions at point P are interpolated by nodal values of the elements containing P using the shape functions:

$$t_i = t_i^c N^c(\xi_1, \xi_2) \quad c = 1,8 \text{ or } 6 \tag{10}$$

The displacement gradients in global and local coordinate systems in the quadratic elements are related by:

$$\frac{\partial u_i(\xi_1,\xi_2)}{\partial \xi_j} = \sum_{c=1}^{8or6} \frac{\partial N^c(\xi_1,\xi_2)}{\partial \xi_j}(u_i)^c = \frac{\partial u_i(\xi_1,\xi_2)}{\partial x_k}\frac{\partial x_k}{\partial \xi_j} \tag{11}$$

Combining Equations (9) and (11), the tractions and displacement gradients in the

local coordinate system can be expressed in terms of global displacements as:

$$\begin{Bmatrix} t_1 \\ t_2 \\ t_3 \\ \frac{\partial u_1}{\partial \xi_1} \\ \frac{\partial u_1}{\partial \xi_2} \\ \frac{\partial u_1}{\partial \xi_3} \\ \frac{\partial u_2}{\partial \xi_1} \\ \frac{\partial u_2}{\partial \xi_2} \\ \frac{\partial u_2}{\partial \xi_3} \end{Bmatrix} = \begin{bmatrix} \frac{2\mu\nu(1-\nu)}{1-2\nu}n_1 & \mu n_2 & \mu n_3 & \mu n_2 & \frac{2\mu\nu}{1-2\nu}n_1 & 0 & \mu n_3 & 0 & \frac{2\mu\nu}{1-2\nu}n_1 \\ \frac{2\mu\nu}{1-2\nu}n_2 & \mu n_1 & 0 & \mu n_1 & \frac{2\mu\nu(1-\nu)}{1-2\nu}n_2 & \mu n_3 & 0 & \mu n_3 & \frac{2\mu\nu}{1-2\nu}n_2 \\ \frac{2\mu\nu}{1-2\nu}n_3 & 0 & \mu n_1 & 0 & \frac{2\mu\nu}{1-2\nu}n_3 & \mu n_2 & \mu n_1 & \mu n_2 & \frac{2\mu\nu(1-\nu)}{1-2\nu}n_3 \\ \frac{\partial x_1}{\partial \xi_1} & 0 & 0 & \frac{\partial x_2}{\partial \xi_1} & 0 & 0 & \frac{\partial x_3}{\partial \xi_1} & 0 & 0 \\ 0 & \frac{\partial x_1}{\partial \xi_1} & 0 & 0 & \frac{\partial x_2}{\partial \xi_1} & 0 & 0 & \frac{\partial x_3}{\partial \xi_1} & 0 \\ 0 & 0 & \frac{\partial x_1}{\partial \xi_1} & 0 & 0 & \frac{\partial x_2}{\partial \xi_1} & 0 & 0 & \frac{\partial x_3}{\partial \xi_1} \\ \frac{\partial x_1}{\partial \xi_2} & 0 & 0 & \frac{\partial x_2}{\partial \xi_2} & 0 & 0 & \frac{\partial x_3}{\partial \xi_2} & 0 & 0 \\ 0 & \frac{\partial x_1}{\partial \xi_2} & 0 & 0 & \frac{\partial x_2}{\partial \xi_2} & 0 & 0 & \frac{\partial x_3}{\partial \xi_2} & 0 \\ 0 & 0 & \frac{\partial x_1}{\partial \xi_2} & 0 & 0 & \frac{\partial x_2}{\partial \xi_2} & 0 & 0 & \frac{\partial x_3}{\partial \xi_2} \end{bmatrix} \begin{Bmatrix} u_{1,1} \\ u_{2,1} \\ u_{3,1} \\ u_{1,2} \\ u_{2,2} \\ u_{3,2} \\ u_{1,3} \\ u_{2,3} \\ u_{3,3} \end{Bmatrix} = [A*]\{u_{k,m}\} \tag{12}$$

Inversion of the matrix **[*A***]** in Equation (12) gives the value of $u_{k,m}$in terms of tractions and displacements at the nodes of the element containing the regularization point P. They are then used in Equations (5), (6) and (8) to calculate the terms for the constant stress state. Using this technique, the singular kernels in Equations (1) and (2) are all regularized and standard Gaussian quadrature can be used to obtain interior point solutions without the need for mesh refinement, even when they are very close to the surface, as will be demonstrated in Section 6.

3 Self-regularized traction-BIE

As proposed in Richardson and Cruse (1999), if an interior point is taken to the boundary so that p and P coincide, Equation (4) becomes

$$\begin{aligned} 0 = &- \int_S S_{kij}(P,Q)[u_k(Q) - u_k^L(Q)]n_i(P)dS(Q) \\ &+ \int_S D_{kij}(P,Q)[t_k(Q) - t_k^L(Q)]n_i(P)dS(Q) \end{aligned} \tag{13}$$

where u_k^L and t_k^L are given before and the unit outward normal $n_i(P)$ is used to reduce the redundancy produced by the index i. This is the self-regularized traction-BIE. Numerical evaluation of the integrals should no longer pose difficulties in principle since they are fully regularized. Methods to deal with the evaluation of singular integrals such as the process of sub-division of elements employed in conventional displacement-BIE are no longer necessary. The terms for the constant stress state, u_k^L and t_k^L, will have to be expressed in terms of nodal values so that the corresponding coefficients can be put into the system matrix. From Equation (12), the displacement gradients can be expressed by nodal tractions and displacements

as:

$$u_{j,m}(P) = A_{kmr}t_r(\xi_1^P, \xi_2^P) + B_{kmr}\sum_{i=1}^{8or6} N_i' u_r^i(\xi_1^P, \xi_2^P) \tag{14}$$

where A_{kmr} contains the first three rows of $[\boldsymbol{A}^*]^{-1}$ and B_{kmr} contains the last six rows, and N_i' are the derivatives of the shape functions at local coordinates ξ_1^P, ξ_2^P corresponding to P. Substituting Equations (14) and (9) into Equations (5) and (6), the constant stress state terms can then be expressed by nodal tractions and displacements as:

$$u_k^L(Q) = u_k(P) + C_{kmr}t_r(\xi_1^P, \xi_2^P) + D_{kmr}\sum_{i=1}^{8or6} N_i' u_r^i(\xi_1^P, \xi_2^P) \tag{15}$$

$$t_k^L(Q) = E_{kmr}t_r(\xi_1^P, \xi_2^P) + F_{kmr}\sum_{i=1}^{8or6} N_i' u_r^i(\xi_1^P, \xi_2^P) \tag{16}$$

where C_{kmr}, D_{kmr}, E_{kmr} and F_{kmr} are third order tensors containing components of $[\boldsymbol{A}^*]^{-1}$ and material constants, which are now put into the system matrix as extra terms.

In the 'relaxed continuity' scheme, the average of the displacement gradients from the different elements sharing the node is taken for u_k^L, as follows,

$$u_k^L(P) = \begin{cases} u_k(P) + u_{k,m}(P)[x_m(Q) - x_m(P)] & forP \in \Delta S \\ u_k(P) + \frac{1}{M}\sum_{j=1}^{M} u_{k,m}(P,j)[x_m(Q) - x_m(P)] & forP \notin \Delta S \end{cases} \tag{17}$$

where M is the number of elements sharing node P, ΔS is the boundary element being integrated, and $u_{k,m}(P,j)$ represents the displacement gradients expressed by nodal tractions and displacements that belong to the j-th element. When ΔS is one of the M elements, no average value is taken but only nodal values belonging to ΔS are involved. The constant stress state tractions t_k^L are defined similarly.

The modified "collocation strategy" moves the collocation points into the interior of the elements where the $C^{1,\alpha}$ continuity requirement is satisfied, instead of at the surface nodes as in conventional BEM. The intrinsic coordinates of the collocation points are set as ξ_1, ξ_2=± 0.9 rather than ± 1 for quadrilateral elements, as illustrated in Figure 1. The displacement gradients at the collocation point, and consequently the constant stress state terms, are expressed in terms of the boundary values of the elements containing the collocation point. For each node shared by M elements, there will be M collocation points, each producing one set of 3 equations. Thus for each node, there will be M sets of equations written onto it to yield only

one set of equations, as when continuous elements are used. This is termed the Multiple Collocation Approach (MCA) by Dominguez and Ariza (2000).

As mentioned earlier, the numerical tests that will be shown later suggest, however, that this self-regularized traction-BIE may not be well-suited for general 3-D elastostatic problems, even though good results have been obtained in 2-D with $C^{0,\alpha}$ elements relaxed continuity scheme as well as with the MCA. The examples will also show that it is not well suited for thin-body problems either, due to the failure of regularization of the singular kernels over the surface that is close to but do not contain the source point P. This will be explained in more detail in Section 6.

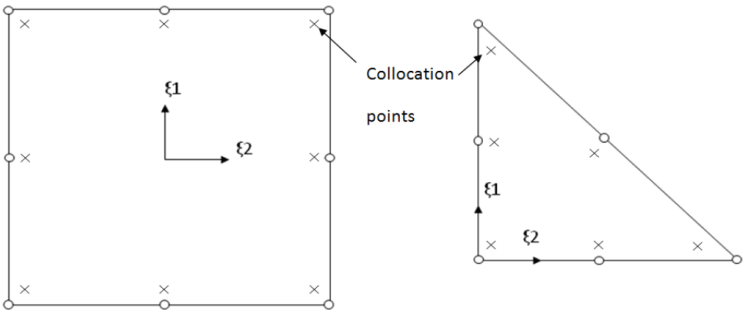

Figure 1: Location of the collocation points inside an element

Inspired by the simplicity of the numerical implementation of the self-regularization scheme and the inadequacy of the traction-BIE to treat the thin-body problem, a new scheme is proposed using the displacement-BIE in this paper; this will be discussed next.

4 A self-regularized displacement-BIE

The self-regularized displacement-BIE proposed in this study adopts the idea of self-regularization but is applied to the displacement-BIE instead. The conventional displacement-BIE is the most commonly used formulation in BEM for stress analysis. The sub-division of the element containing the source point P when integrating the strongly singular kernels is kept as in conventional displacement-BIE to regularize these kernels; those elements that are very close to but not containing $P$are regularized using the proposed scheme below.

The displacement-BIE is written as

$$C_{ij}(P)u_j(P) + \int_S T_{ij}(P,Q)u_j(Q)dS(Q) = \int_S U_{ij}(P,Q)t_j(Q)dS(Q) \tag{18}$$

where P and Q are source and field points on the surface S of the elastic domain, respectively, and $C_{ij}(P)$ is the free term. In the notion of self-regularization, some terms corresponding to a constant stress state need to be subtracted from Equation (18). For a reference point P_0 on the surface, the displacement-BIE for constant stress state expression at P_0 can be written as

$$C_{ij}(P)u_j^L(P_0,P)+\int_S T_{ij}(P,Q)u_j^L(P_0,Q)dS(Q)=\int_S U_{ij}(P,Q)t_j^L(P_0,Q)dS(Q) \tag{19}$$

where the constant stress terms are expressed as

$$u_j^L(P_0,P)=u_j(P_0)+u_{j,m}(P_0)[x_m(P)-x_m(P_0)] \tag{20}$$

$$u_j^L(P_0,Q)=u_j(P_0)+u_{j,m}(P_0)[x_m(Q)-x_m(P_0)] \tag{21}$$

$$t_j^L(P_0,Q)=\sigma_{jm}(P_0)n_m(Q) \tag{22}$$

Subtracting Equation (17) from (16) yields

$$\begin{aligned} &C_{ij}(P)[u_j(P)-u_j^L(P_0,P)]+\textstyle\int_S T_{ij}(P,Q)[u_j(Q)-u_j^L(P_0,Q)]dS(Q)\\ &=\textstyle\int_S U_{ij}(P,Q)[t_j(Q)-t_j^L(P_0,Q)]dS(Q)\end{aligned} \tag{23}$$

Similar to the traction-BIE, the constant stress state terms u_k^L and t_k^L need to be expressed in terms of nodal displacements and tractions of the element containing P_0 so that the corresponding coefficients can be placed in the system matrix. The procedure is the same as before except that in Equations (14) to (16), P is now P_0 and Q can be either Q or P. The following expressions are thus obtained:

$$u_j^L(P_0,PorQ)=\sum_{i=1}^{8or6}N_i'u_j^i(\xi_1^{P_0},\xi_2^{P_0})+C_{kmr}t_r(\xi_1^{P_0},\xi_2^{P_0})+D_{kmr}\sum_{i=1}^{8or6}N_i'u_r^i(\xi_1^{P_0},\xi_2^{P_0}) \tag{24}$$

and

$$t_j^L(Q)=E_{kmr}t_r(\xi_1^{P_0},\xi_2^{P_0})+F_{kmr}\sum_{i=1}^{8or6}N_i'u_r^i(\xi_1^{P_0},\xi_2^{P_0}) \tag{25}$$

Note that the shape functions N_i in Equations (24) and (25) have been changed to those corresponding to local coordinates of P_0 in the element containing P_0. Substituting Equations (24) and (25) into Equation (23), the system equations may be obtained in the usual manner.

In conventional displacement-BIE, the values for the free term C_{ij} which represent (3 x 3) sub-matrices located at the diagonal of the system matrix [$\boldsymbol{A}$], are usually

obtained indirectly by considering the rigid-body motion condition. In Equation (23), however, C_{ij} appears not only at the diagonal sub-matrices of $[\boldsymbol{A}]$, but also in the columns corresponding to P_0 with the opposite sign. If the off-diagonal coefficients in each line of matrix $[\boldsymbol{A}]$ are summed up as in conventional BEM, the C_{ij} terms at these two places will cancel each other. The rigid-body motion condition thus cannot beused for calculating the C_{ij} terms here. An alternative approach of direct evaluation of the free terms is thus employed, which will be described in the next section.

The regularization point P_0 is located close to the source point P but does not share the same element with P, as shown in Figure 2. This ensures that the regularization point is located on the second nearest surface containing the near singularities when dealing with thin-body problems. Using this self-regularization technique, the displacement-BIE in Equation (23) can be used for treating thin-body problems without the need of very significant mesh refinement as in conventional BEM analysis.

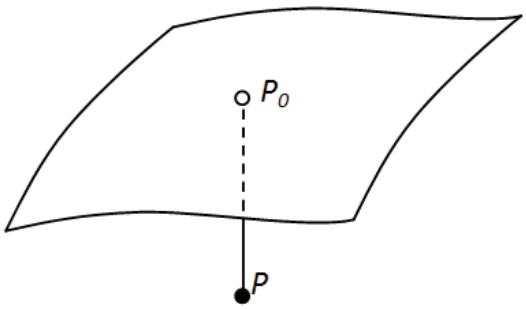

Figure 2: Location of the regularization point P_0

5 Evaluation of $\mathbf{C}_{ij}$

The numerical values of the components of C_{ij} may be obtained following the analytical approach introduced by Dangla, Semblat, Xiao and Delepine (2005) as described in the Appendix. They depend on the local geometry at P. These analytically obtained C_{ij} sub-matrices are always symmetric. However, because of numerical modeling with discrete elements, the computed values of C_{ij} are not exactly symmetric in practical BEM meshes, unless the source point is shared by perfectly square elements, which is seldom the case in practice. Tests show, however, that using the analytically obtained C_{ij} terms for general problems can sometimes

result in significant errors; thus, this analytical approach may not be entirely suitable. A numerical scheme is proposed here to deal with this difficulty in which a small auxiliary model based on the elements sharing P is created. These elements sharing P are projected to a plane a distance L to P with L being the largest distance between P and the nodes of the elements sharing P. The direction of the projection is the opposite direction of the average outward normal at P, $\overrightarrow{n}(P)$.

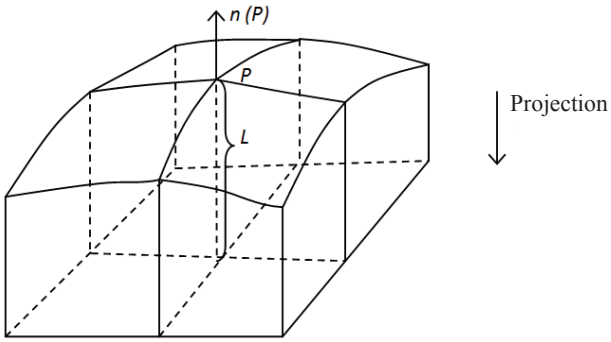

Figure 3: Schematic diagram of the auxiliary model based on elements around node P, the source point.

The C_{ij} values can now be calculated using rigid body motion on the auxiliary model as in conventional BEM. When dealing with thin-body problems, however, at some of the nodes, the corresponding auxiliary model will become another thin body, such as the mid-side node Aat the short edge of a thin plate shown in Figure 4. In this case, the analytical approach in Dangla, Semblat, Xiao and Delepine (2005) is used instead. In the BEM computer code used in this study, if a node is shared by an element having an aspect ratio larger than 3, the C_{ij} terms at this node will be calculated using the analytical approach; for smaller aspect ratios, the C_{ij} values will be obtained using the numerical integration over the auxiliary model. Tests show that this approach provides accurate solutions for both thick and thin bodies.

6 Numerical examples

Several numerical examples are presented here to demonstrate the respective self-regularization algorithms described in the previous sections. The implementation has been carried out with modifications made to an existing BEM code for 3-D isotropic elastostatics in which 4x4 Gauss and 13-points Hammer-Stroud quadratures are employed for quadrilateral and triangular elements, respectively. Examples (A) and (B) demonstrate the efficiency and accuracy of the self-regularization

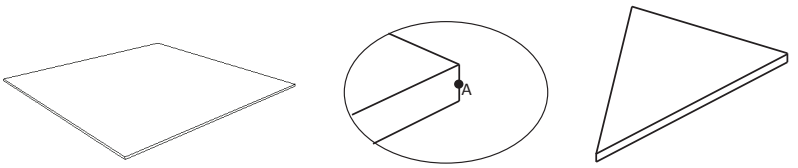

a) original model - a thin plate b) mid-node *A* c) auxiliary model of node *A*

Figure 4: a) original model - a thin plate b) mid-node A c) auxiliary model of node A

technique in interior point solutions in 3-D as discussed in Section 2. Examples (C) and (D) provide tests using the self-regularized traction-BIE and adopting the relaxed continuity and the multiple collocation strategies. Finally, Examples (E) and (F) will illustrate the performance of the proposed self-regularized displacement-BIE when dealing with thin-body problems. Analysis using the conventional BEM is also carried out on each of these problems, as well as with the finite element method for some cases, for the purpose of comparison of the corresponding results.

6.1 Interior point solutions

Example (A): The first example considered for obtaining interior point solutions is a cantilever beam subject to a unit shear load on the free end. The beam has a length of 8 units and square cross-section of side length 1 unit, as shown in Figure 5. Young's modulus was set to 1000 units and Poisson's ratio to zero to enable comparison with the results of one-dimensional simple beam theory. The mesh used has 72 elements and 218 nodes. Interior points were arbitrarily chosen to be located along a central line in the cross-section 3 units from the fixed end. The interior points were deliberately located as close to the upper and lower surfaces of the beam for the purpose of this exercise, the distance to the surface reducing to as low as 0.0001unit.

The results obtained using the BEM, with and without the self-regularization technique, are listed in Table 1 and compared with the corresponding values from simple beam theory. As can be seen, the results obtained using self-regularization scheme remains very accurate even as the interior point is very close indeed to the boundary, while with the conventional BEM code with the same fixed quadrature, the stress results begin to deteriorate very sharply when the distance reaches 0.1from the surface; this being so because the singularity of the kernels in the integrals for the stresses is one order higher than that of the displacements.

Example (B): A thick-walled spherical vessel under internal pressures is consid-

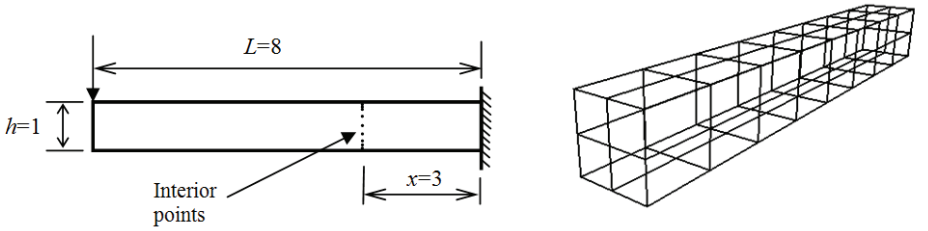

Figure 5: Problem definition and mesh discretization: Example (A)

Table 1: Displacements and stresses at interior points: Example (A)

	Axial stress			Vertical displacement		
y	Beam Theory	Self-reg.	Without Self-reg.	Beam Theory	Self-reg.	Without Self-reg.
0.4999	-29.994	-29.640	-7879.0	0.378	0.380	0.191
0.499	-29.940	-29.586	-7791.4	0.378	0.380	0.197
0.49	-29.400	-28.804	-1537.3	0.378	0.380	0.269
0.4	-24.000	-23.538	-103.7	0.378	0.380	0.381
0.2	-12.000	-11.786	-11.8	0.378	0.380	0.380
0	0.000	0.000	0.00	0.378	0.380	0.380
-0.2	12.000	11.786	11.8	0.378	0.380	0.380
-0.4	24.000	23.539	103.7	0.378	0.380	0.381
-0.49	29.400	28.805	1537.3	0.378	0.380	0.269
-0.499	29.940	29.587	7791.4	0.378	0.380	0.197
-0.4999	29.994	29.641	7879.0	0.378	0.380	0.191

ered next (see Figure 6); it has inner and outer radii of 2 and 3 units, respectively. Young's modulus was set to 1000 units and Poison's ratio was taken to be 0.3. Due to symmetry, only one-eighth of the problem was modeled with 48 elements and 148 nodes (see Figure 6). Also shown in the figure are a series of interior points arbitrarily located from inner surface to the outer surface along a radial plane. Table 2 lists the results obtained from the BEM analysis with and without the self-regularization, and compared with the well-known Lame's exact solution. Again, the use of self-regularization yields very accurate results even when the interior point is close to either of the surfaces with standard integration scheme; no special transformation or further mesh refinement was required.

Table 2: Principal stresses and radial displacements of the pressurized sphere: Example (B)

	σ_1			σ_2			σ_3			Radial displacement, u_r		
r	Exact	Self-reg.	Without self-reg.	Exact	Self-reg.	Without self-reg.	Exact	Self-reg.	Without self-reg.	Exact	Self- reg.	Without self-reg.
2.001	1.131	1.121	144080	1.131	1.099	48620	-0.998	-0.980	23350	2.143E-03	2.183E-03	9.18E-02
2.01	1.121	1.115	1772	1.121	1.095	1669	-0.979	-0.969	-9387	2.134E-03	2.168E-03	5.67E-02
2.1	1.035	1.046	2.985	1.035	1.038	2.840	-0.807	-0.812	-7.420	2.010E-03	2.029E-03	2.21E-03
2.5	0.785	0.792	0.784	0.785	0.790	0.784	-0.307	-0.326	-0.306	1.602E-03	1.603E-03	1.60E-03
2.9	0.654	0.653	13.595	0.654	0.648	-2.681	-0.045	-0.040	-2.790	1.362E-03	1.367E-03	1.84E-03
2.99	0.634	0.641	13808	0.634	0.634	-2505	-0.004	-0.008	-2917	1.321E-03	1.330E-03	7.76E-02
2.999	0.632	0.640	-8737	0.632	0.633	-29729	0.000	-0.006	-58414	1.319E-03	1.327E-03	6.67E-02

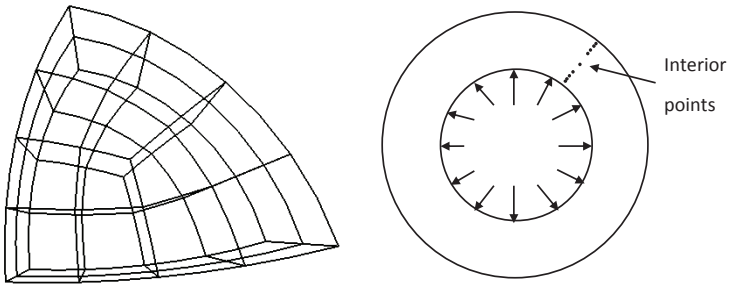

Figure 6: Problem definition and mesh discretization: Example (B)

6.2 Boundary solutions with the self-regularized traction-BIE

Example (C): The first example for the self-regularized traction-BIE is a thick-walled cylinder with a radius ratio of 2 and unit height, subject to axial loading and internal pressure separately. Taking advantage of symmetry, only one-quarter of the physical problem is modeled, as shown in Figure 7. The results for a series of nodes along two vertical lines on the inner and outer surfaces are observed. For the axial loading case for which the stresses are uniform throughout the domain, both the relaxed continuity approach and multiple collocation strategy gave very good results, as shown in Table 3. However, in the internal pressure load case for which the stress distributions in the cylinder are not uniform, the relaxed continuity approach was found to produce very unsatisfactory results; they are therefore not presented here. The results obtained from the multiple collocation approach (MCA) and from the conventional displacement-BIE are shown in Table 4. The MCA satisfies better the continuity requirement, since collocation points are always within the elements. However, the results are still not very accurate, with errors exceeding 10%. The serious errors in these two schemes are found to be caused by the presence of the corners in the model. This suggests that neither of them can sufficiently meet the continuity requirement of the displacement-gradients across element boundaries, especially at corners. No further tests on a thin-walled cylinder are therefore conducted.

Example (D): To establish that the errors in Example $(C)$are indeed due to the presence of geometric corners in the BEM model, an internally pressurised sphere is then tested using the full geometry, as shown in Figure 8. It has 48 elements and 148 nodes. The numerical results are compared with the well-known Lame's exact analytical solution. Figure 9 and Tabel 10 present the variations of the maximum errors in the stresses and displacements, respectively, with the radius ratio Kranging

Table 3: Stress results for the cylinder under axial loading: Example (C)

	Relaxed continuity						Multiple Collocation Approach					
Location	Outer surface			Inner surface			Outer surface			Inner surface		
z	σ_1	σ_2	z	σ_1	σ_2	σ_3	σ_1	σ_2	σ_3	σ_1	σ_2	σ_3
0	1.003	-6.5E-04	-6.5E-04	1.010	-1.4E-03	-1.4E-03	1.000	-2.4E-05	-2.4E-05	1.000	7.8E-05	7.8E-05
0.125	1.016	4.4E-03	4.4E-03	1.003	-1.1E-03	-1.1E-03	1.000	-1.8E-05	-1.8E-05	1.000	-1.2E-05	-1.2E-05
0.25	1.000	-3.1E-03	-3.1E-03	1.004	-1.9E-03	-1.9E-03	1.000	-1.2E-05	-1.2E-05	1.000	1.8E-06	1.8E-06
0.375	0.998	-3.2E-03	-3.2E-03	1.004	-9.6E-04	-9.6E-04	1.000	-1.0E-05	-1.0E-05	1.000	6.0E-07	6.0E-07
0.5	0.999	-8.0E-03	-8.0E-03	0.981	-1.2E-02	-1.2E-02	1.000	-1.3E-05	-1.3E-05	1.000	3.7E-07	3.7E-07
0.625	0.999	-8.1E-04	-8.1E-04	0.996	3.5E-03	3.5E-03	1.000	-1.5E-05	-1.5E-05	1.000	-2.5E-06	-2.5E-06
0.75	1.000	-4.4E-04	-4.4E-04	1.009	1.1E-02	1.1E-02	1.000	-7.8E-06	-7.8E-06	1.000	1.2E-07	1.2E-07
0.875	1.000	-1.9E-03	-1.9E-03	1.009	1.2E-02	1.2E-02	1.000	5.9E-07	5.9E-07	1.000	-3.7E-07	-3.7E-07
1	1.002	-1.9E-03	-1.9E-03	1.009	1.3E-02	1.3E-02	1.000	-2.7E-05	-2.7E-05	1.000	1.3E-05	1.3E-05
Exact	1.000	0.00	0.00	1.00	0.00	0.00	1.00	0.00	0.00	1.00	0.00	0.00

Table 4: Stress results for the thick-walled cylinder under internal pressure: Example (C)

	Conventional Displacement-BIE						Multiple Collocation Approach					
	Outer surface			Inner surface			Outer surface			Inner surface		
z	σ_1	σ_2	σ_3	σ_1	σ_2	σ_3	σ_1	σ_2	σ_3	σ_1	σ_2	σ_3
0	0.6745	0.1960	0.0372	1.6886	0.1857	-0.9017	0.7237	0.1913	-0.0186	1.7298	0.3583	-0.7312
0.125	0.6640	0.1993	0.0001	1.6631	0.1991	-0.9995	0.7587	0.2175	0.0001	1.7260	0.2377	-0.9995
0.25	0.6639	0.1984	0.0001	1.6635	0.2002	-0.9995	0.7547	0.2295	0.0001	1.7051	0.2019	-0.9995
0.375	0.6640	0.1992	0.0001	1.6631	0.1992	-0.9995	0.7732	0.2422	0.0001	1.7797	0.2147	-0.9994
0.5	0.6639	0.1991	0.0001	1.6631	0.1990	-0.9995	0.7624	0.2444	0.0001	1.7180	0.1869	-0.9995
0.625	0.6640	0.1992	0.0001	1.6742	0.2031	-0.9995	0.7732	0.2422	0.0001	1.7797	0.2147	-0.9994
0.75	0.6639	0.1984	0.0001	1.6635	0.2001	-0.9995	0.7547	0.2295	0.0001	1.7051	0.2015	-0.9995
0.875	0.6640	0.1993	0.0001	1.6634	0.1991	-0.9995	0.7587	0.2175	0.0001	1.7251	0.2373	-0.9995
1	0.6745	0.1960	0.0372	1.6889	0.1861	-0.9003	0.7237	0.1913	-0.0185	1.7295	0.3607	-0.7251
Exact	0.667	0.200	0.000	1.667	0.200	0.000	0.667	0.200	0.000	1.667	0.200	0.000

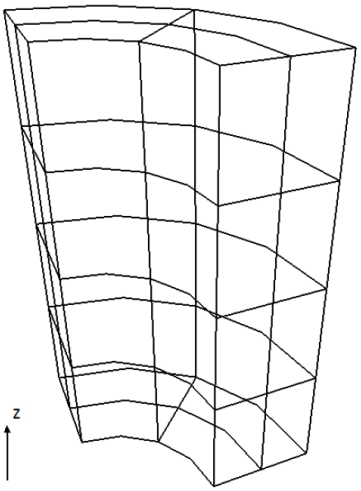

Figure 7: BEM mesh of the thick-walled cylinder: Example (C)

from 1.1 to 2.

The results show that with the absence of corners, the traction-BIE provides even better results (less than 2%) than the displacement-BIE when K is high, with either the relaxed continuity or multiple collocation strategy. When the thickness of the hollow sphere reduces, however, the accuracy of the traction-BIE algorithms starts to degenerate even faster than the displacement-BIE, and no convergence is observed with mesh refinement. This suggests that when stresses are not uniformly distributed within the body, even with the absence of corners, the BEM formulation using the traction-BIE is not able to recover good results for the thin-walled sphere.

The above two examples are part of a more extensive range of simple problems that have been tested with the traction-BIE formulation. It appears that the convergence of the results is not always assured for 3-D problems when corners are present in spite of the schemes aimed at trying to satisfy the continuity requirement for the displacement gradients across inter-element boundaries. In the axial loading case for Example (C) treated here, it involves only uniform stress and no stress discontinuity is present, thus the results remain very accurate. In the internal pressure load case, however, it suffers from the discontinuity of the displacement gradients at the edges of the cylinder ends, giving rise to the errors in the results near there. Dramatic mesh refinement, as has been carried out in previous 2-D studies (e.g.

Richardson and Cruse (1999)) that had yielded convergence of the solutions using this approach is cost prohibitive n 3-D. It is therefore questionable if the self-

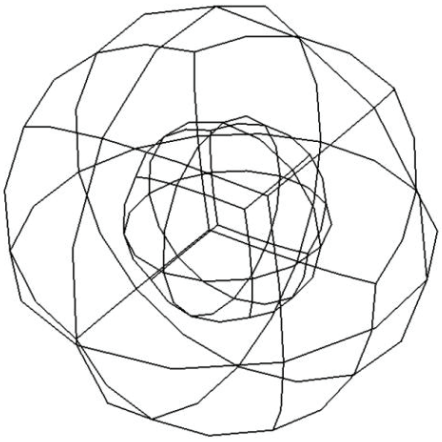

Figure 8: BEM mesh of the hollow sphere subject to internal pressure: Example (D)

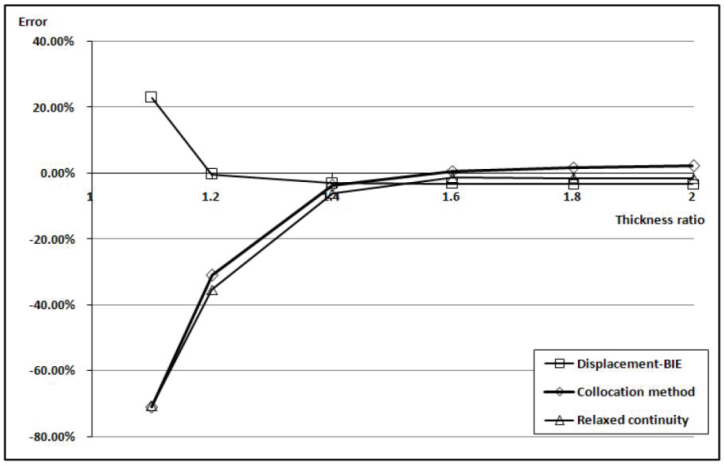

Figure 9: Variation of maximum error in stresses with radius ratio of the hollow sphere: Example (D)

regularized traction-BIE here can be well suited for 3-D general elastostatic problems unless an analytically simple scheme is developed to ensure stress continuity around geometry corners. The same can be said of its use for treating thin-body problems. This can be argued as follows with reference to Figure 11: the self-regularization adopted in this scheme only regularizes the singular kernels at field

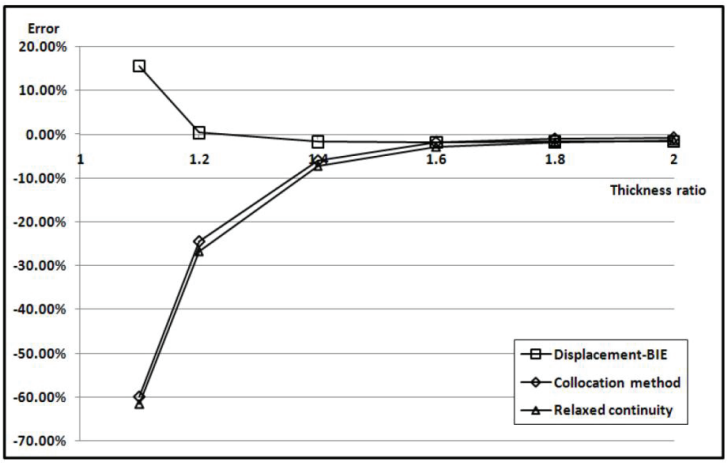

Figure 10: Variation of maximum error in displacements of the hollow sphere: Example (D)

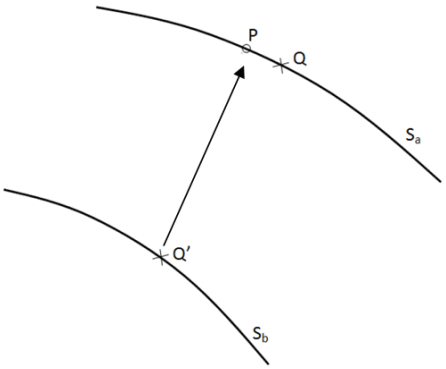

Figure 11: Schematic diagram of the location of source point P and the surfaces S_a and S_b

points Qon the surface S_a containing source point $P$by the constant stress terms at P itself. When dealing with thin-body problems, another surface S_b is very close to P as well, but the singular kernels at a field point Q' on this surface cannot be regularized using Pas the regularization point. This explains the dramatic drop in accuracy for the solutions in Example (D) as the radius ratio of the sphere is decreased to 1.1.

6.3 Boundary solutions with the self-regularized displacement-BIE

Example (E): The thin-walled pressurized cylinder and sphere are the first set first set of thin-body problems considered here. The regularization points of the nodes on the inner/outer surface are the closest points located on the opposing surface to regularize the singular kernels. Taking advantage of symmetry, only one-quarter of the thin-walled cylinder is modeled. The initial BEM mesh for the cylinder is shown in Figure 12a; it has 38 elements and 116 nodes. The inner radius of the cylinder is set at unity while the outer radius is reduced from 1.1 to 1.001, so that the thickness t decreases from 0.1 to 0.001. The results at a series of nodes on the inner surface located from the bottom ($z/H = 0$) to the top surface ($z/H = 1$) are examined. The accuracy of the results deteriorates with the mesh used when thickness reduces to 0.001. To establish that it is indeed due to the extraordinarily large aspect ratios of the element dimensions of those used to model the cylinder ends (524:1) and the radial planes of symmetry (333:1), a refined mesh, as shown in Figure 12b is tested for this case. It has 160 elements and 482 nodes. The errors in the stresses at the nodes on the inner surface for cases of *t=0.1, 0.01* and 0.001are shown in Figure 13.

As shown in the results, the stresses at the nodes on the smooth surface generally have less than 2% error. For the nodes at the corners, i.e., when $z/H = 0$or $z/H = 1$, however, the errors in radial stresses are found to be very high. This was again established to be due to the large aspect ratio of the elements representing the wall thickness. To verify this, a partially refined mesh for the case of $t = 0.1$ is tested, as shown in Figure 14. The aspect ratios of the elements across the wall thickness are reduced to be close to unity. With this mesh, the errors in radial stresses at every node decreased to be less than 3%.

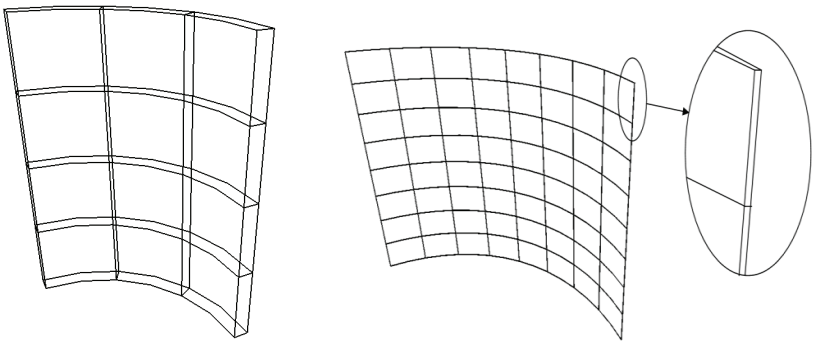

(a) Initial mesh (b) Refined mesh

Figure 12: BEM meshes for the thin-walled cylinder

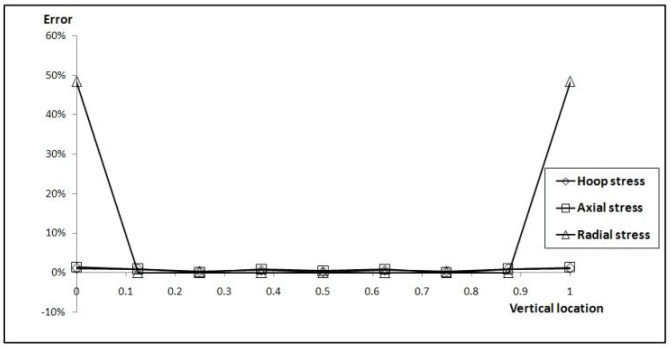

(a) *t=0.1*

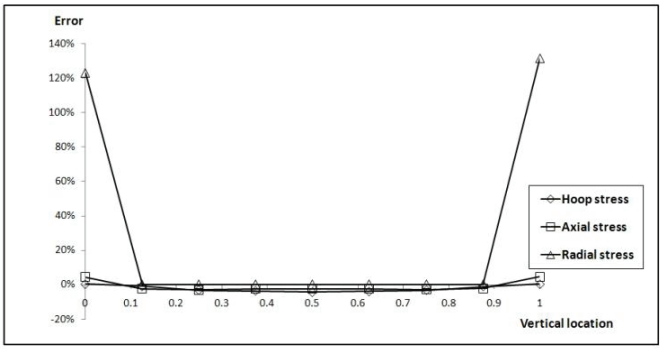

(b) *t=0.01*

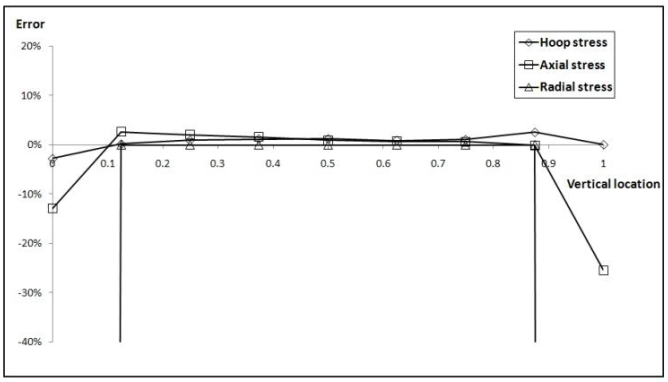

(c) *t=0.001* (refined mesh)

Figure 13: Percentage errors of the computed stresses at the nodes for the thin-walled cylinders

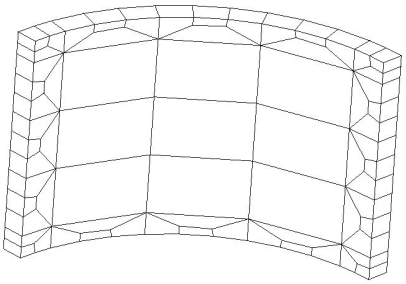

Figure 14: A radial plane of a tapered cylinder

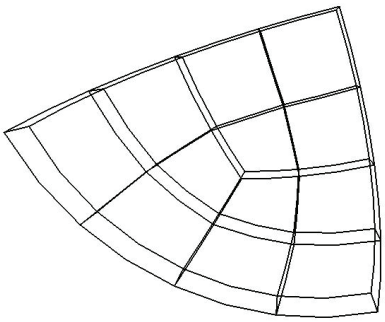

Figure 15: BEM mesh for the thin-walled sphere

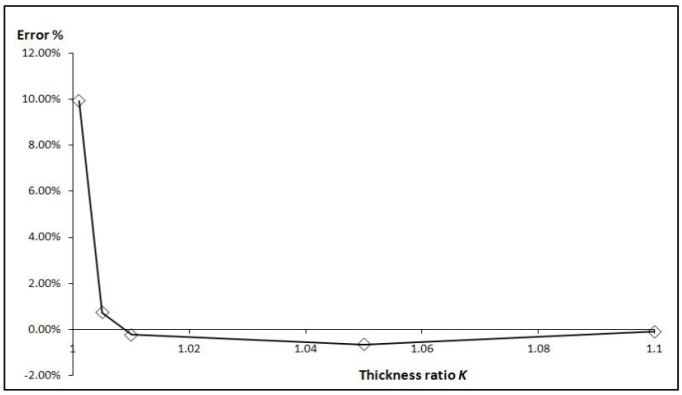

Figure 16: Variation of the maximum errors in the circumference stress with the thickness ratio K for the pressurized thin-walled sphere problem

The BEM mesh for the thin-walled sphere is shown in Figure 15. Only one-eighth of the sphere is modeled by taking advantage of symmetry; it has 36 elements and 110 nodes. The inner radius is kept at unity, and the thickness t is reduced from 0.1 to 0.001 so that the thickness ratio K decreases from 1.01 to 1.001. As discussed above, the stresses at the corners have relatively high errors due to the very large aspect ratio of the elements representing the wall thickness, thus only those on the smooth surface are investigate. Figure 16 show the maximum error of the circumferential stresses at an arbitrary node on the inner surface with the variation of the thickness ratio K. the regularized displacement-BIE gives less than 3% error for thickness up to 0.005 and starts to deteriorate at t=0.001. This is, again, due to the large aspect ratio of the elements across the wall thickness. In comparison, the conventional BIE is also tested on these examples and was found to fail from t=0.1, demonstrating the efficiency and accuracy of the proposed self-regularized displacement-BIE when dealing with thin-body problems. It should perhaps be noted that when using the finite element method with solid elements to treat such problems, very refined meshes will also be needed to maintain a reasonable aspect ratio of the element dimensions, unless a judicious choice of shell elements is made for the analysis.

Example (F): A very useful application of the proposed self-regularized displacement-BIE algorithm is for treating physical problems which cross-sections varying from very thick to relatively thin. Two examples involving varying thicknesses are considered here for illustration. They are, namely, a pressurized tapered cylinder, and an ellipsoid containing a spherical cavity under pressure. As no analytical solutions are readily available, finite element analysis is conducted using very refined meshes to check the accuracy of the solutions obtained using the BEM. Although both problems are axisymmetric, the 3-D BEM analysis is performed as tests for the algorithm developed. Figure 17 shows the radial plane of cylinder with linearly varying thickness; it is subject to an internal pressure of unity. The inner radius of the cylinder is kept at unity while the outer radius is linearly decreased from 1.5 at the bottom to a smaller value $r$at the top. Three cases are treated here, namely, r=*1.05, 1.01,* and 1.005.

Figure 18 shows the typical finite element mesh of the problem using axisymmetric elements. The mesh around the thinner part of the model is refined as $r$decreases to ensure accuracy. As a test of the 3-D BEM code, only one-quarter of the physical problem is modeled in the BEM analysis. As r is decreased, the aspect ratio of the elements at the top surface increases, thus the mesh there is refined accordingly. Figure 19 shows a series of three gradually refined meshes, which are all tested to observe the convergence of the results.

The maximum circumferential stress occurs at the top inner surface of the cylinder

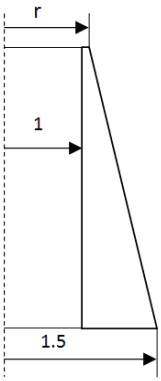

Figure 17: A radial plane of a tapered cylinder

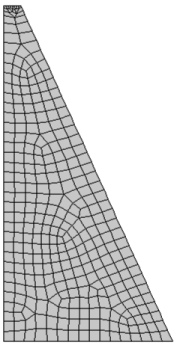

Figure 18: Finite element mesh of the cylinder with varying thickness (320 Elements; 3059 nodes)

and only its results are presented for the sake of brevity. They are listed in Table 5 where those obtained from FEM and the BEM using the three different meshes, with and without self-regularization are compared. It can be seen that as the aspect ratio of the elements at the top surface decreases, the self-regularized displacement-BIE gives results very close to the FEM results. The conventional BIE, on the other hand, produces results with higher discrepancies as r decreases. It should be pointed out that both the self-regularized and conventional BIE gave accurate results at the thick portion of the models.

The cross-section of a pressurized ellipsoid is shown in Figure 20 with the z-axis as an axis of revolution. The vessel has a spherical cavity with radius, a, under unit pressure, the outer surface of the cross-section has an elliptical profile, the

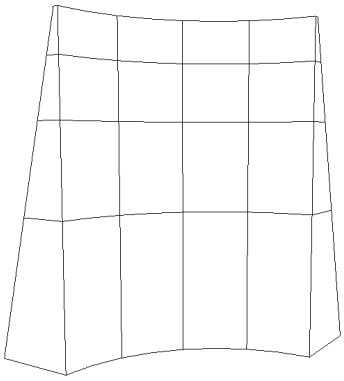

(a) Mesh #1: 4 elements across top surface

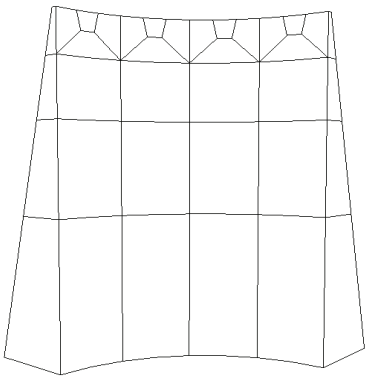

(b) Mesh #2: 12 elements across top surface

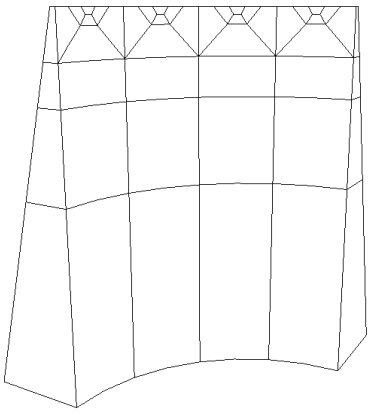

(c) Mesh #3: 20 elements across top surface

Figure 19: BEM meshes for the pressurized tapered cylinder

Table 5: Maximum stress in the pressurized cylinder with varying thickness

r	FEM	No. of elements across top surface	BEM (with regularization)	BEM (without regularization)
1.05	15.23	4	14.34	14.25
		12	14.79	14.87
		20	14.88	14.72
1.01	39.01	4	34.03	27.53
		12	34.65	31.44
		20	37.77	27.72
1.005	50.98	4	43.58	-494.53
		12	46.61	71.58
		20	51.92	99.18

Table 6: Hoop stresses in the pressurized ellipsoid

c/a		FEM	BEM	Conventional BEM
1.05	Point A	9.440	9.159	9.725
	Point B	3.080	3.109	3.175
1.01	Point A	46.867	44.677	54.073
	Point B	3.268	3.151	3.162
1.005	Point A	93.655	89.495	170.30
	Point B	3.2938	3.2408	3.2369

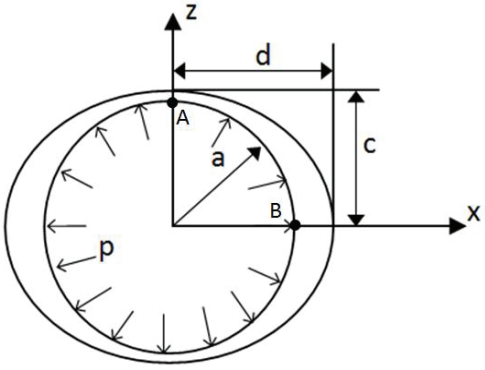

Figure 20: Cross-section of an ellipsoid with a pressurized spherical cavity

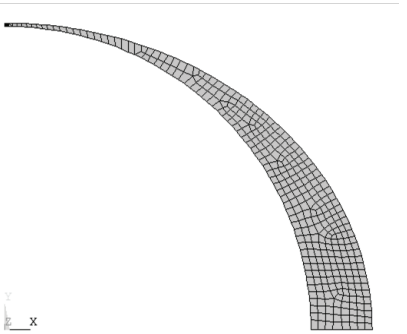

Figure 21: FEM mesh of the pressurized ellipsoid

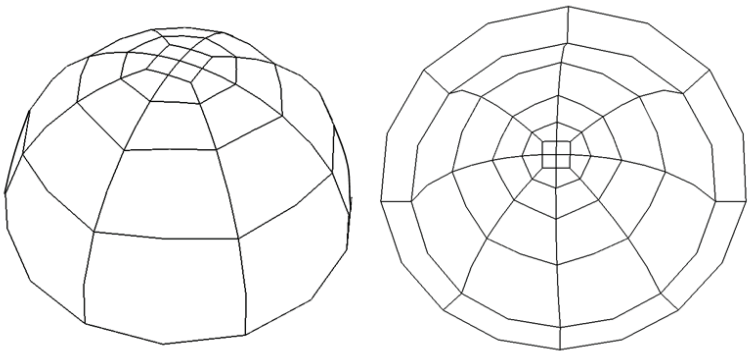

(a) Top view (b) Bottom view

Figure 22: BEM mesh of the pressurized ellipsoidal vessel

semi-major axis being $c$and the semi-minor axis, d.The ratio c/a is kept at 1.2 while $d/a$is varied from 1.05, 1.01 to 1.005. The axisymmetric finite element mesh used for the purpose of comparison of the results is shown in Figure 21; it has 431 elements and 1480 nodes. The BEM mesh employed is shown in Figure 22, with 88 elements and 266 nodes. The half model with symmetry about the horizontal plane is employed to avoid further discussion on the large aspect ratios that would occur at the thin portion if a quarter-model is used instead.

Table 6 lists the hoop stresses at points A and B from the FEM, and BEM analyses, with and without the self-regularization. As can be seen in the table, very good agreement with the FEM results are obtained with the self-regularized displacement-BIE algorithm of the BEM using the relatively coarse mesh, while with the conventional BEM, the accuracy deteriorates as c/a decreases.

These two examples demonstrate that the self-regularized displacement-BIE can provide very accurate solutions for geometries with continuously varying thickness irrespective of whether it is thin or thick, provided due care is taken with the BEM model to avoid excessive aspect ratios of the element dimensions.

7 Conclusions

In this paper, the self-regularization technique proposed in Cruse and Richardson (1996) and Richardson and Cruse (1999) in 2-D BEM stress analysis has been extended to 3-D. It has been first implemented to obtain interior point solutions in the three-dimensional solid domain and excellent accuracy of the numerical results is maintained even when the interior point is very close to the surface of the domain with relative coarse mesh and fixed quadrature schemes. This is unlike with the use of conventional displacement-BEM. Using the same strategies that have been previously suggested in 2-D analysis, the self-regular traction-BIE has also been extended to 3-D elasostatics. However, the numerical tests undertaken in this study suggest that unless a more efficient and accurate means is found to preserve the smoothness requirements of displacement gradients across the element boundaries, the use of $C^{0,\alpha}$ conforming elements with the traction-BIE developed in Cruse and Richardson (1996) and Richardson and Cruse (1999) cannot ensure convergence of accurate solutions. Neither is this scheme suited for treating thin-body problems due to the near singularities that occur by the presence of the second surface nearby.

A self-regularized displacement-BIE has been proposed in this study that provides a very effective tool to treat thin-body problems that neither the conventional BEM nor the self-regularized traction-BIE algorithm is well suited for. Numerical examples have been presented to demonstrate the efficiency of this scheme with BEM using standard quadratic isoparametric elements and fixed integration schemes. Due care to avoid excessive aspect ratio of the element dimensions need to be taken, however, to ensure consistent accurate results are obtained throughout the solution domain.

Appendix

An analytical expression for the free term in the displacement-BIE, C_{ij}, has been derived by Dangla, Semblat, Xiao and Delepine (2005). It is given as follows:

$$C_{ij}(P) = \frac{\psi}{4\pi}\delta_{ij} - \frac{1}{8\pi(1-\nu)}\sum_{e=1}^{E}\sin(\frac{\theta^e}{2})(b_i^e n_j^e + b_j^e n_i^e) \tag{A-1}$$

where $E$is the number of elements sharing the node P, $\theta^e$is the angle formed by the two edges of element e at P, b_i^e is the unit vector of the bisecting line of these

two edges, and n_i^e is the unit outward normal of element e. These quantities are illustrated in Figure A-1, with a unit sphere centered at P. The solid angle ψ can be calculated using

$$\psi = \sum_{e=1}^{E} (\psi_1^e + \psi_2^e + \psi_3^e - \pi) \tag{A-2}$$

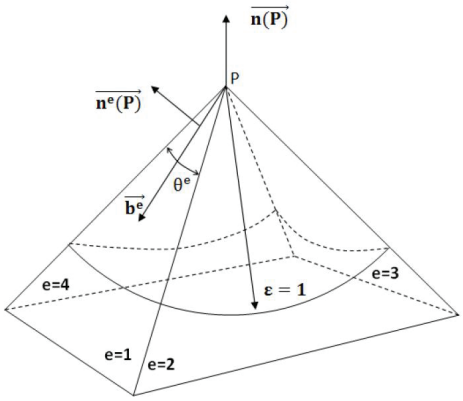

Figure A-1: Schematic of elements sharing node P

where ψ_i^e are the angles formed by the planes of the trihedron as shown in the figure. This trihedron is formed by the two edges of element e, the semi-axis in the direction of $-n(P)$, and the part of the unit sphere cut off by these three lines, where $n(P)$ is an arbitrarily chosen normal at P, usually taken as the average of outward normal of the elements sharing P. It was suggested that the choice of this $n(P)$ does not affect the accuracy of the free term as the solid angle will be recovered whatever the $n(P)$ is. Since $n(P)$ is the average of the normal of the elements sharing P, its opposite will always be located between the edges of the elements. Thus, the sum of ψ_3^e will become 2π, and Equation (A-2) becomes

$$\psi = \sum_{e=1}^{E} (\psi_1^e + \psi_2^e) + 2\pi - E\pi) \tag{A-3}$$

To obtain the angles ψ_i^e, we need the vectors $\boldsymbol{v}_i$ as shown in Figure A-2. These vectors are obtained as follows:

$$\begin{aligned} \vec{v}_1 &= \vec{n}^e \times \vec{a}_1 \\ \vec{v}_2 &= \vec{a}_1 \times (\vec{n}(P) \times a_1) \\ \vec{v}_3 &= \vec{a}_2 \times \vec{n}^e \\ \vec{v}_4 &= \vec{a}_2 \times (\vec{n}(P) \times \vec{a}_2) \end{aligned} \tag{A-4}$$

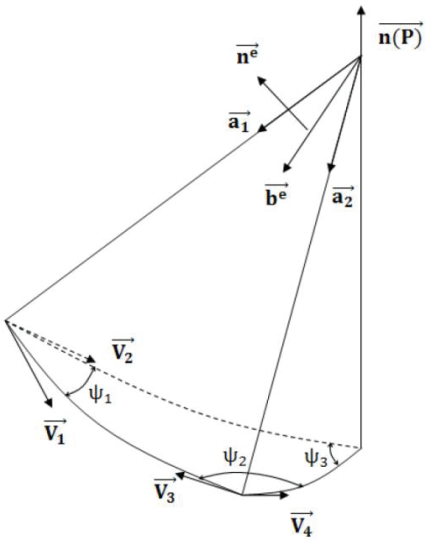

Figure A-2: Illustration figure for solid angle ψ

where $\vec{a}_1$ and $\vec{a}_2$ are the unit vectors of the two edges. ψ_i^e can now be obtained by:

$$\begin{aligned} \psi_1 &= \cos^{-1}\left(\frac{\vec{v}_1 \vec{v}_2}{|\vec{v}_1||\vec{v}_2|}\right) \\ \psi_2 &= \cos^{-1}\left(\frac{\vec{v}_3 \vec{v}_4}{|\vec{v}_3||\vec{v}_4|}\right) \end{aligned} \tag{A-5}$$

Once all the quantities in Equation (A-1) are obtained, the explicit terms C_{ij} can be computed and appropriately placed into the system matrix corresponding to the node P and nodes of the elements containing P_0.

References

Cruse, T. A. (1969): Numerical solutions in three dimensional elastostatics. *International Journal of Solids and Structures*, vol. 5, pp. 1259-1274.

Cruse, T. A.; Aithal, R. (1993): Non-singular boundary integral equation implementation. *International Journal for Numerical Methods in Engineering*, vol. 36, pp. 237-254.

Cruse, T. A.; Richardson, J. D. (1996): Non-singular Somigliana stress identities in elasticity. *International Journal for Numerical Methods in Engineering*, vol. 39, no. 19, pp. 3273-3304.

Dangla, P.; Semblat, J. F.; Xiao, H.; Delepine, N. (2005): A simple and efficient

regularization method for 3-D BEM: Application to frequency-domain elastodynamics. *Bulletin of the Seismological Society of America,* vol. 95, no. 5, pp. 1916-1927.

Dominguez, J.; Ariza, M. P. (2000): A direct traction-BIE approach for three-dimensional crack problems. *Engineering Analysis with Boundary Elements,* vol. 24, pp. 727-738.

Dong, L.; Atluri, S. N. (2012): SGBEM (using non-hyper-singular traction-BIE) and super elements, for non-collinear fatigue-growth analyses of cracks in stiffened panels with composite-patch repairs. *CMES Computer Modeling in Engineering & Sciences*, vol. 89, no. 5, pp. 415-456.

Frangi, A.; Guiggiani, M. (2001): Free terms and compatibility conditions for 3D hypersingular boundary integral equations. *ZAMM: Zeitschrift für Angewandte Mathematik und Mechanik,*vol.81, no.10, pp.651–664.

Jin, Z. R.; Zhang, D. M.; Wang, Y. H.; Li, Z. L.; (2011): Dynamic element discretization method for solving 2-D traction boundary integral equations. *Engineering Analysis with Boundary Elements*, vol. 35, no. 11, pp, 1204-1213.

Jorge, A. B.; Cruse, T. A.; Fisher, T. S;. Ribeiro, G. O.; (2003): A new varietional self-regular traction-BEM formulation for inter-element continuity of displacement derivatives. *Computational Mechanics,* vol. 32, no. 4-6, 401-414.

Krishnasamy, G.; Rizzo, F. J.; Li, Y. J. (1994): Boundary integral equations for thin bodies. *International Journal for Numerical Method in Engineering*, vol. 37, pp. 107-121.

Li, J. (2003): *The evaluation of T-stress using boundary element method.* M. A. Sc. Thesis, Carleton University.

Liu, Y. J. (1987): Elastic stability analysis of thin plate by the boundary element method – a new formulation. *Engineering Analysis with Boundary Elements*, vol. 4, pp. 160-164.

Liu, Y. J. (1998): Anlysis of shell-like structures by the boundary element method based on 3-D elasticity: formulation and verification. *International Journal for Numerical Methods in Engineering.,* vol. 41, pp. 541-558.

Ma, H.; Kamiya, N.; (2001): A general algorithm for accurate computation of field variables and its derivatives near the boundary in BEM. *Engineering Analysis with Boundary Elements*, vol. 25, no. 10, pp. 833-841.

Martin, P. A.; Rizzo, F. J. (1996): Hypersingular integrals: how smooth must the density be? *International Journal for Numerical Methods in Engineering,* vol. 39, pp. 687-704.

Martin, P. A.; Rizzo, F.; Cruse, T. A. (1998): Smoothness-relaxation strategies for

singular and hypersingular integral equations. *International Journal for Numerical Methods in Engineering,* vol. 42, pp. 885-906.

Matsumoto, T.; Tanaka, M. (1993): Boundary stress calculation using regularized boundary integral equation for displacement gradients. *International Journal for Numerical Methods in Engineering*, vol. 36, pp. 783-797.

Niu, Z.; Wendland, W. L.; Wang, X.; Zhou, H.; (2005): A semi-analytical algorithm for the evaluation of the nearly singular integrals in three-dimensional boundary element methods. *Computer Methods in Applied Mechanics and Engineering*, vol. 194, no. 9-11, pp. 1057-1074.

Richardson, J. D.; Cruse, T. A. (1999): Weakly singular stress-BEM for 2-D elastostatics. *International Journal for Numerical Methods in Engineering*, vol. 45, pp. 13-35.

Rudolphi, T. J. (1991): The use of simple solutions in the regularization of hypersingular boundary integral equations. *Mathematical and Computer Modeling*, vol. 15, pp. 269-278.

Shah, P. D.; Tan, C. L.; Wang, X. (2006): T-stress solutions for two-dimensional crack problems in anisotropic elasticity using the boundary elements method. *Fatigue & Fracture of Engineering Materials & Structures*, vol. 29, no. 5, pp. 343-356.

Sladek, V.; Sladek, J.; Tanaka, M. (1993): Regularization of hypersingular and nearly singular integrals in potential theory and elasticity. *International Journal for Numerical Methods in Engineering*, vol. 36, pp. 1609-1628.

Wang, Ch.; Li, Z. L. (2009): Application of relations of singularity intensities of tangent derivatives of boundary displacements and tractions to BEM. *Engineering Analysis with Boundary Elements*, vol. 33, pp. 618-626.

Xie, G.; Zhang, J. M.; Qin, X. Y.; Li, G. Y.(2011): New variable transformations for evaluating nearly singular integrals in 2-D boundary element method. *Engineering Analysis with Boundary Elements*, vol. 35, no. 6, pp. 811-817.

Ye, T. Q.; Liu, Y. J. (1985): Finite deflection analysis of elastic plate by the boundary element method. *Applied Mathematical Modelling*, vol. 9, pp. 183-188.

Yu, J. (2006): *T-stress solutions of cracks emanating from circular holes*, M. A. Sc. Thesis, Carleton University, Ottawa, Ontario, Canada.

Zhou, H. L.; Niu, Z. R.; Cheng, C. Z.;. Guan, Z. W. (2008): Analytical integral algorithm applied to boundary layer effect and thin body effect in BEM for anisotropic potential problems. *Computers and Structures*, vol. 86, pp. 1656-1671.